Postprint of Variational Model for Interactive Buckling of Thin-Walled I-Section Members with Nonlinear Materials

Authors: Zhang Jinyi

Date: 2025-11-01T00:00:00+00:00

Abstract

Cold-formed thin-walled members are highly susceptible to interactions among multiple instability modes, and research on the coupled buckling mechanical mechanisms for members with various cross-sectional shapes and material types urgently requires improvement and development. An accurate variational model for slender thin-walled I-section members was established, comprehensively accounting for material nonlinearity, geometric nonlinearity, global initial geometric imperfections, and the connection stiffness between flanges and webs. This model was employed to analyze coupled buckling and post-buckling load-displacement curves, ultimate bearing capacity, and plate local buckling waves. The results demonstrate that the nominal yield strength of the material significantly influences the member' s post-buckling bearing capacity, while global initial imperfections substantially affect the ultimate bearing capacity but have a relatively minor impact on post-buckling bearing capacity. The plate local buckling wavelength decreases as the post-buckling bearing capacity declines. The variational model was used to simulate existing experiments, showing high agreement between simulation and experimental results, thereby validating the model' s accuracy. The model reveals the complete mechanical mechanism of nonlinear global-local coupled buckling in thin-walled members, providing a theoretical foundation for both research and design.

Full Text

Preamble

Vol. 42 No. 5 Oct. 2025

Chinese Journal of Applied Mechanics DOI: 10.11776/j.issn.1000-4939.2025.05.006

Variational Model on Mode Interaction in Long I-Section Struts with Material Nonlinearity

ZHANG Jinyi[1,2], BAI Li[1,2], WANG Yingyi[1], YANG Jian[1,2], WANG Feiliang[1,2]

[1]. School of Naval Architecture, Ocean and Civil Engineering, Shanghai Jiao Tong University, Shanghai 200240, China
[2]. Shanghai Key Laboratory for Digital Maintenance of Building and Infrastructure, Shanghai 200240, China

Abstract: Cold-formed thin-walled members are highly susceptible to the interaction of multiple buckling modes, necessitating further development of research on the mechanical mechanisms of interactive buckling across different cross-sectional forms and material types. This study establishes an accurate variational model for thin-walled I-section slender members that comprehensively accounts for material nonlinearity, geometric nonlinearity, global initial geometric imperfections, and the connection stiffness between flanges and webs. Based on this model, the interactive buckling and post-buckling load-displacement curves, ultimate bearing capacities, and local buckling waves are analyzed. The results demonstrate that the nominal yield strength of materials significantly influences the post-buckling capacity of members. Global initial imperfections substantially affect the ultimate bearing capacity but have minimal impact on post-buckling capacity. The local buckling wavelength of plates decreases as the post-buckling capacity declines. The variational model is used to simulate existing experiments, and the simulation results show excellent agreement with experimental data, thereby validating the model' s accuracy. The model reveals the complete mechanical mechanism of nonlinear global-local interactive buckling in thin-walled members, providing a theoretical foundation for research and design.

Keywords: structural stability; thin-walled member; mode interaction; material nonlinearity; Ramberg-Osgood model
Classification: TU392

Introduction

Cold-formed thin-walled members exhibit three fundamental buckling modes: plate local buckling, cross-sectional distortional buckling, and member global buckling [1-3]. Under certain conditions, coupling between different buckling modes can occur, significantly affecting load-bearing capacity and post-buckling performance [4-6]. In recent years, numerous scholars have investigated the interactive buckling behavior of thin-walled members with various cross-sectional forms, including lipped channels [7-9], box sections [10-11], angle sections [12-13], I-sections [14-15], and stiffened plates [16-17]. Most existing literature employs ideal elastic-plastic or multi-linear constitutive models without a yield plateau

for member materials. However, for nonlinear metallic materials such as stainless steel [18] and aluminum alloys [19], the stress-strain curves are smooth and continuous without a distinct yield plateau [20]. While many researchers have studied the stability of nonlinear metallic material members through experimental and numerical methods [21-22], analytical studies remain scarce, and most existing analytical research considers only a single buckling mode [23]. Some scholars have introduced the nonlinear Ludwick constitutive model in analytical studies [24], but few have considered the Ramberg-Osgood (R-O) constitutive model [25] for nonlinear metallic materials, primarily because strain is an irreversible function of stress in the R-O model, making theoretical derivation highly challenging. BAI et al. [26] established a variational model for interactive buckling in long rectangular hollow section struts considering the R-O model, demonstrating that material mechanical properties significantly influence interactive buckling. Finite element simulations validated the model with excellent agreement. WADEE et al. [27] and BAI et al. [28] investigated the effects of initial geometric imperfections on the interactive buckling behavior and load-bearing capacity of linear material thin-walled I-section members using analytical methods. BAI et al. [29] analytically studied the influence of flange-web connection stiffness on interactive buckling in linear material thin-walled I-section struts, while references [26-28] employed a simplified hinge connection between flanges and webs.

Given the limited analytical research on interactive buckling in thin-walled members made of nonlinear metallic materials, and the absence of analytical methods considering both global initial imperfections and material nonlinearity, this study employs the Rayleigh-Ritz method to develop a variational model for interactive buckling failure modes in thin-walled I-section slender members with simply supported ends. The model comprehensively incorporates geometric nonlinearity, material nonlinearity (R-O model), global initial imperfections, and varying connection stiffness between flanges and webs. By calculating the complete load-displacement curves and plate buckling waves for interactive and post-buckling behavior, the study investigates the influence of material mechanical properties and imperfection amplitudes on post-buckling performance, aiming to provide a theoretical foundation and reference data for research and design formula improvements regarding interactive buckling in thin-walled members made of nonlinear materials. BECQUE [30] conducted experimental studies on the interactive buckling behavior of thin-walled I-section stainless steel members and simulated the tests using finite element software. This research compares the variational model results with both the experimental and finite element results from [30] to validate the model' s effectiveness.

1. Material Constitutive Model

The classical continuous constitutive model for nonlinear metallic materials is the Ramberg-Osgood model, originally proposed in its initial form [25] as:

$$\varepsilon = \frac{\sigma}{E_0} + K\sigma^n$$

where E_0 is the initial Young' s modulus and n is the material hardening coefficient. HILL [31] modified this into the classical R-O model:

$$\varepsilon = \frac{\sigma}{E_0} + 0.002\left(\frac{\sigma}{\sigma_{0.2}}\right)^n$$

where $\sigma_{0.2}$ is the nominal yield strength. Combining equations (1) and (2) yields $\sigma_{0.2} = E_0(0.002/K)^{1/n}$, making parameter K equivalent to the nominal yield strength. Introducing the linear strain component $\varepsilon_L = \sigma/E_0$ and substituting into equation (1) gives:

$$\varepsilon = \varepsilon_L + K\varepsilon_L^n$$

Equation (3) represents the relationship between strain and its linear component for ideal members made of nonlinear materials, with the stress-strain curve shown in [FIGURE:1]. By extension, assuming the shear strain and its linear component satisfy $\gamma = \gamma_L + K(\gamma_L)^n$, where $\gamma_L = \tau/G_0$ and G_0 is the initial shear modulus.

2. Variational Model Establishment

This study employs the Rayleigh-Ritz method by first assuming continuous displacement functions for global and local plate buckling modes, then deriving the strain energy and total potential energy expressions. The equilibrium differential equations and integral boundary conditions are obtained through Euler-Lagrange equations and stationary functional conditions. Finally, the complete interactive buckling load-displacement curves and local buckling waves are solved. The model solution involves continuation and bifurcation of differential equation solutions, computed using the software AUTO [32].

2.1 Continuous Displacement Functions

Thin-walled I-section slender members are formed by joining two C-section components. Axial compression is uniformly transferred to the cross-section through rigid end plates. The member can freely bend about either the strong or weak axis, with remaining boundary conditions and cross-sectional parameters shown in [FIGURE:2].

For slender members, the critical stress for global buckling about the weak axis is typically lower than the critical stress for plate local buckling. Since the web thickness is twice that of the flange and the web is constrained on four sides while the flange is constrained on three sides with one free edge, the web' s critical

buckling stress is significantly higher than that of the flange. Therefore, the web is assumed not to undergo local buckling. During loading, global buckling occurs first, causing compression in the flange on one side of the web (referred to as the compressed flange) and tension in the flange on the opposite side (referred to as the tension flange). Subsequently, the compressed flange undergoes local buckling, forming a global-local mode coupling interaction, while the tension flange does not experience local buckling. The tension flange is assumed to be hinged to the web, while the compressed flange is connected to the web through a torsional spring, as shown in FIGURE:3.

In practical engineering, the connection stiffness between flanges and webs ranges from zero to positive infinity and can be simulated using torsional spring stiffness c. For cold-formed thin-walled members, the corner region is equivalent to a torsional spring, with an effective flange length of $2b_e$, as shown in FIGURE:3.

The stiffness c is estimated using a simplified method. Assuming the corner region is a flat plate under uniformly distributed bending moment in the longitudinal direction, the transverse deflection is w_c, with its x_{cw} end connected to the web and x_{cf} end connected to the flange. The relative rotation between flange and web at their connection equals the relative rotation between sections x_{cf} and x_{cw}. For a unit-length plate, $d_c^{2w}/dx_c^2 = M/D_c$ is constant, where $D_c = E_{c0} \cdot t^3/[12(1-\nu^2)]$ is the initial stiffness of the corner region and E_{c0} is the initial elastic modulus of the corner region. Therefore, the relative rotation $\theta_{wf} = ML_c/D_c$, where $L_c = 2^{1/2}r$ is the equivalent width of the flat plate. Since c is the moment provided by the spring per unit rotation:

$$c = \frac{D_c}{L_c} = \frac{E_{c0}t^3}{12(1-\nu^2) \cdot 2^{1/2}r}$$

For the global buckling mode, considering Euler-Bernoulli beam theory, the global lateral displacement is assumed as $W(z)$ with its linear component $W_L(z)$. Assuming $W_L(z) = Q_L \sin(\pi z/L)$, where Q is the dimensionless amplitude of the displacement curve. The simplified bending strain-displacement relationship $\varepsilon = x/R = x(d^{2W}/dz^2)$ is adopted, where R is the radius of curvature. The linear component satisfies $\varepsilon_L = x/R_L = x(d_L^{2W}/dz^2)$. For ideal members, substituting the strain-displacement relationship into equation (3) yields:

$$\frac{d^{2W}}{dz^2} = \frac{d_L^{2W}}{dz^2} + Kx^{n-1}\left(\frac{d_L^{2W}}{dz^2}\right)^n$$

Substituting W_L into equation (5) and integrating with respect to x, then based on boundary conditions $W(0) = 0$ and symmetry condition $W'(L/2) = 0$, the indefinite integral with respect to z gives:

$$W(z) = Q_L \sin\frac{\pi z}{L} + \frac{Kb^n}{(n+1)2^n}\left(\frac{\pi}{L}\right)^{2n} Q_L^n \int_0^z \int_0^\zeta f(x)dxd\zeta$$

The cross-section rotation θ satisfies $\theta = dW/dz$, with its linear component θ_L assumed to satisfy $\theta_L = dW_L/dz$. Global bending causes longitudinal displacements in flanges and webs: $u_\theta = -x\theta$, with linear component $u_{\theta L} = -x\theta_L$. The global buckling lateral displacement and cross-section rotation are shown in [FIGURE:4].

Assuming the member develops global initial imperfections before normal service but without initial stress, as shown in [FIGURE:5]. The initial lateral displacement is $W_0 = Q_{0L}\sin(\pi z/L)$ and initial cross-section rotation $\theta_0 = Q_0\pi\cos(\pi z/L)$. For members with geometric imperfections, the incremental longitudinal displacement in flanges and webs under global bending is $u_\theta = -x(\theta - \theta_0)$, with linear component $u_{\theta L} = -x(\theta_L - \theta_0)$.

For the local buckling mode, the out-of-plane displacement function of the compressed flange $w(x,z)$ is assumed as $f(x)w(z)$, as shown in FIGURE:6, where $f(x)$ and $w(z)$ represent transverse and longitudinal displacement components, respectively. This study employs the following $f(x)$ expression derived from deflection curve equations of simply supported and cantilever beams [29]:

$$f(x) = -\frac{s_2}{2b_e}x^2 + \frac{s_4}{\pi}\sin\frac{\pi x}{b_e} + s_6$$

where $s_2 = -s_0\pi b_e/4$, $s_4 = 2s_{0b}e/\pi$, $s_0 = 1/(\pi D - b_{ec})$, $s_6 = 1 - s_2 + s_4$. $D = E_{0t}^3/[12(1-\nu^2)]$ represents the initial plate stiffness. When $c = 0$, $f(x)$ is a linear function; when c approaches infinity, the flange and web are rigidly connected, as shown in FIGURE:3, and $f(x)$ becomes:

$$f(x) = -\frac{4\pi - \pi^2 - 8}{2\pi^2}\left(\frac{x}{b_e}\right)^2 + \frac{8}{\pi^2}\sin\frac{\pi x}{2b_e}$$

The in-plane longitudinal displacement function of the compressed flange is assumed as $u(x,z) = -(2x/b)u(z)$, as shown in FIGURE:6, neglecting in-plane transverse displacement. The linear components of out-of-plane and in-plane displacements are introduced as $w_L(x,z) = f(x)w_L(z)$ and $u_L(x,z) = -(2x/b)u_L(z)$, respectively.

2.2 Total Potential Energy Formulation

The total potential energy of the member comprises global strain energy, local plate strain energy, torsional spring strain energy, and external load work. Local plate strain energy includes bending strain energy and membrane strain energy. Notably, global strain energy considers only web bending strain, while

flange bending strain due to global bending is included in membrane strain energy. Geometric nonlinearity is considered in membrane strain energy using the Green-Lagrange strain tensor. Due to the complexity of formulation derivation, this study employs the scientific computing software MATHEMATICA for assistance.

2.2.1 Global Strain Energy The strain energy density formula differs between nonlinear and linear materials. Under global bending, neglecting shear strain, differentiate equation (1) with respect to σ, substitute $d\varepsilon$ into the strain energy density differential formula $dU_\rho = \sigma d\varepsilon$, then integrate with respect to σ [26] to obtain:

$$U_\rho = \frac{\sigma^2}{2E_0} + \frac{K\sigma^{n+1}}{n+1}$$

For ideal members, substituting $\varepsilon_L = \sigma/E_0$ into equation (9) yields the strain energy density:

$$U_\rho = \frac{E_0\varepsilon_L^2}{2} + \frac{KE_0^{n+1}\varepsilon_L^{n+1}}{n+1}$$

For members with geometric imperfections, assuming initial strain ε_0, the incremental strain during normal service is $(\varepsilon - \varepsilon_0)$ with linear component $(\varepsilon_L - \varepsilon_0) = \sigma/E_0$. Substituting this into equation (9) gives:

$$U_\rho = \frac{E_0(\varepsilon_L - \varepsilon_0)^2}{2} + \frac{KE_0^{n+1}(\varepsilon_L - \varepsilon_0)^{n+1}}{n+1}$$

Substituting the global bending strain-displacement relationship, W_L and W_0 into equation (11) and integrating over the web volume yields the global strain energy U_B:

$$U_B = E_0 \int_0^L \left[\frac{(Q-Q_0)^2\pi_w^{4I}}{4L^4} \sin^2\frac{\pi z}{L} + \frac{K\pi^{2n+2}I_{w,n+1}}{(n+1)L^{2n+2}} \sin^{n+1}\frac{\pi z}{L} \right] dz$$

where I_w represents the second moment of area of the web about the weak axis, $I_w = \int x^2 dA$; $I_{w,n+1}$ is defined as the $(n+1)$th moment of the web area, $I_{w,n+1} = \int x^{n+1} dA$, with A representing the web cross-sectional area.

2.2.2 Local Plate Strain Energy Local plate strain energy comprises bending strain energy and membrane strain energy. First, the local strain energy density formula is determined. Using the compressed flange as an example and assuming plane stress, longitudinal normal strain ε_z, transverse normal strain ε_x, and shear strain γ_{xz} are considered, along with their linear components ε_{Lz},

ε_{Lx}, and γ_{Lxz}. Extending the one-dimensional R-O model to two dimensions yields:

$$\begin{bmatrix}\varepsilon_z\\ \varepsilon_x\\ \gamma_{xz}\end{bmatrix}=\frac{1}{E_0}\begin{bmatrix}1 & -\nu & 0\\ -\nu & 1 & 0\\ 0 & 0 & 2(1+\nu)\end{bmatrix}\begin{bmatrix}\sigma_z\\ \sigma_x\\ \tau_{xz}\end{bmatrix}+K\begin{bmatrix}(\sigma_z-\nu\sigma_x)^n\\ (\sigma_x-\nu\sigma_z)^n\\ [2(1+\nu)\tau_{xz}]^n\end{bmatrix}$$

where ν is Poisson' s ratio. Setting the linear strain component vector $[\varepsilon_{Lz},\varepsilon_{Lx},\gamma_{Lxz}]^T$ equal to the first term on the right side of equation (13) and rewriting the second term using the linear strain-stress relationship, analogous to equation (3), yields the relationship between strain vector and its linear components. Extending the one-dimensional strain energy density equation (9) to three dimensions gives the plate strain energy density formula [26]:

$$U_\rho=\frac{E_0}{2(1-\nu^2)}\left[\varepsilon_{Lx}^2+\varepsilon_{Lz}^2+2\nu\varepsilon_{Lx}\varepsilon_{Lz}+\frac{1-\nu}{2}\gamma_{Lxz}^2\right]+\frac{KE_0^{n+1}}{n+1}\left[(\varepsilon_{Lx}+\nu\varepsilon_{Lz})^{n+1}+(\varepsilon_{Lz}+\nu\varepsilon_{Lx})^{n+1}+\frac{1-\nu}{2}\gamma_{L}^{n}\right.$$

1) Plate Bending Strain Energy

Flange bending strain energy adopts small deformation assumptions. The bending strain-displacement relationships are $\varepsilon_x=-y(\partial^{2w}/\partial x^2)$, $\varepsilon_z=-y(\partial^{2w}/\partial z^2)$, and $\gamma_{xz}=-2y[\partial^{2w}/(\partial x\partial z)]$. The linear components maintain similar relationships:

$$\varepsilon_{Lx}=-y\frac{\partial_L^{2w}}{\partial x^2},\quad \varepsilon_{Lz}=-y\frac{\partial_L^{2w}}{\partial z^2},\quad \gamma_{Lxz}=-2y\frac{\partial_L^{2w}}{\partial x\partial z}$$

Substituting equation (15) into equation (14) and integrating over the compressed flange volume yields the flange bending strain energy U_b:

$$U_b=\int_0^L\int_{-b_e}^{b_e}\left\{\frac{D}{2}\left[\left(\frac{\partial_L^{2w}}{\partial x^2}\right)^2+\left(\frac{\partial_L^{2w}}{\partial z^2}\right)^2+2\nu\frac{\partial_L^{2w}}{\partial x^2}\frac{\partial_L^{2w}}{\partial z^2}+2(1-\nu)\left(\frac{\partial_L^{2w}}{\partial x\partial z}\right)^2\right]+\frac{KD_{n+1}}{n+1}\left[\left(\frac{\partial_L^{2w}}{\partial x^2}+\nu\frac{\partial_L^{2w}}{\partial z^2}\right)^{n+1}\right.\right.$$

where $D=E_{0t}^3/[12(1-\nu^2)]$ and $D_{n+1}=E_{0t}^{n+2}/[2^{n+1}(n+2)(1-\nu^2)^n]$.

Substituting the bending strain-displacement relationships and equation (15) into the strain vector-linear component relationship and integrating over the flange thickness yields the relationship between out-of-plane displacement w and its linear component w_L:

$$\frac{\partial^{2w}}{\partial z^2}=Kt^{n-1}\left[\frac{\partial_L^{2w}}{\partial x^2}+\nu\frac{\partial_L^{2w}}{\partial z^2}\right]^n+\frac{\partial_L^{2w}}{\partial z^2}$$

2) Plate Membrane Strain Energy

In the post-buckling stage, plate displacements exceed small deformation limits, generating membrane strain energy. Geometric nonlinearity is considered using the Green-Lagrange strain tensor and von Kármán large deflection theory. For plate transverse normal strain, only Poisson' s effect is assumed: $\varepsilon_{Lx} = -\nu\varepsilon_{Lz}$. For plate longitudinal normal strain, axial compressive strain $\Delta + K\Delta^n$ and its linear component Δ are introduced. Flange longitudinal normal strain also includes a strain term from displacement u_θ. Large shear deformation occurs only in the compressed flange during post-buckling. Substituting plate normal and shear strains into the strain energy density equation (14) and integrating over plate volume yields membrane strain energy $U_m = U_d + U_s$, where U_d represents membrane strain energy from normal strain and U_s from shear strain.

The membrane strain energy U_d is calculated as:

$$U_d = \frac{E_{0t}}{n+1}\int_0^L \int_{-b/2}^{b/2} \left[\varepsilon_{Lz,c}^{n+1} + \varepsilon_{Lz,t}^{n+1}\right] dxdz + \frac{E_{0t_{wh}}}{n+1}\int_0^L \varepsilon_{Lz,w}^{n+1} dz$$

The linear strain-displacement formulas for compressed and tension flanges are:

$$\varepsilon_{Lz,c} = -\Delta + \frac{\partial u_L}{\partial z} - \frac{1}{2}\left(\frac{\partial w_L}{\partial z}\right)^2 - x\frac{d\theta_L}{dz}, \quad \varepsilon_{Lz,t} = -\Delta - x\frac{d\theta_L}{dz}$$

For members with global initial imperfections, $u_{\theta L} = -x(\theta_L - \theta_0)$.

The shear strain energy U_s is:

$$U_s = \frac{G_{0t}}{n+1}\int_0^L \int_{-b/2}^{b/2} \gamma_{Lxz}^{n+1} dxdz$$

The linear shear strain-displacement for the compressed flange is:

$$\gamma_{Lxz} = \frac{\partial u_L}{\partial x} + f(x)f'(x)w_{Lw}L'$$

In equations (19) and (21), the last two terms of $\varepsilon_{Lz,c}$ and γ_{Lxz} are based on von Kármán large deflection theory.

2.2.3 Torsional Spring Strain Energy The strain energy of torsional springs attached to the upper and lower compressed flanges is:

$$U_{sp} = \int_0^L \frac{c}{2}\left[\frac{\partial w(x,z)}{\partial x}\right]^{2dx}$$

After trial calculations, replacing function w with w_L in equation (22) reduces computational complexity while maintaining solution accuracy. Furthermore, torsional spring strain energy has minimal influence on total potential energy V and model results.

2.2.4 External Load Work The external load work P_E includes axial deformation from global bending, local plate displacement, and axial compressive strain:

$$P_E = P\int_0^L \left[\frac{1}{2}W'^2 + (\Delta + K\Delta^n) + \frac{1}{2bt + ht_w}\int_{-b/2}^{b/2}\left(\frac{\partial u(x,z)}{\partial z} + \frac{1}{2}\left(\frac{\partial w(x,z)}{\partial z}\right)^2\right)dx\right]dz$$

where $u(x,z)$ and its linear component $u_L(x,z)$ satisfy $\partial u(x,z)/\partial z = \partial u_L(x,z)/\partial z + K[\partial u_L(x,z)/\partial z]^n/n$. The integral average with respect to x yields $u' = u'_L + K(u'_L)^n/n$. W' is calculated using equation (6). For members with global geometric imperfections, the actual axial deformation is E from equation (23) minus the initial axial deformation E_0, as shown in [FIGURE:5]. However, the initial axial deformation constant is eliminated during subsequent equilibrium equation derivation, so it is not presented in equation (23).

The total potential energy V is the combination of these strain energies:

$$V = U_B + U_b + U_d + U_s + U_{sp} - P_E$$

which can be written in functional form as:

$$V = \int_0^L F(z, w_L, w'_L, w''_L, u_L, u'_L)dz$$

2.3 Derivation of Equilibrium Differential Equations and Boundary Conditions

The first variation of total potential energy δV is:

$$\delta V = \int_0^L \left[\frac{\partial F}{\partial w_L}\delta w_L + \frac{\partial F}{\partial w'_L}\delta w'_L + \frac{\partial F}{\partial w''_L}\delta w''_L + \frac{\partial F}{\partial u_L}\delta u_L + \frac{\partial F}{\partial u'_L}\delta u'_L\right]dz$$

In equilibrium, total potential energy V must be stationary, leading to the following Euler-Lagrange equations:

$$\frac{\partial F}{\partial w_L} - \frac{d}{dz}\frac{\partial F}{\partial w'_L} + \frac{d^2}{dz^2}\frac{\partial F}{\partial w''_L} = 0, \quad \frac{\partial F}{\partial u_L} - \frac{d}{dz}\frac{\partial F}{\partial u'_L} = 0$$

Equation (27) yields the equilibrium differential equation system of the variational model: a fourth-order nonlinear differential equation for w_L and a second-order nonlinear differential equation for u_L. Based on simply supported boundary conditions and symmetry:

$$w(0) = w_L(0) = w''(0) = w'(L/2) = w'_L(L/2) = u(L/2) = u_L(L/2) = u'(0) = u'_L(0) = 0$$

In equilibrium, the model must also satisfy stationary functional conditions, leading to integral boundary conditions $\partial V/\partial Q = 0$ and $\partial V/\partial \Delta = 0$.

After nondimensionalization of some variables based on displacement symmetry (e.g., $\bar{z} = 2z/L$, $\bar{w}_L = 2w_L/L$, $\bar{u}_L = 2u_L/L$), the software AUTO [32] is used to obtain numerical solutions of the equilibrium differential equation system under boundary conditions. Solutions for half-span loads and displacements are obtained, then extended to the full span using symmetry. After obtaining solutions for displacement linear components w_L and u_L and their derivatives, displacement w and u and their derivatives are calculated using relationships such as equation (17).

2.4 Numerical Solution Process

For perfect members, model solution involves three stages (solution continuation) and two bifurcation points, as shown in FIGURE:7. External load P gradually increases to the critical load P_C (Stage 1), triggering global buckling (first bifurcation point C). After branching at point C, global lateral displacement Q develops (Stage 2) until local buckling is triggered and couples with global buckling (second bifurcation point S). Branching at point S enters the post-interactive buckling stage (Stage 3), where member capacity drops rapidly.

For members with global initial imperfections, the solution process includes two stages and one bifurcation point, as shown in FIGURE:7. External load P increases from zero (Stage 1), with global lateral displacement Q increasing from initial imperfection amplitude Q_0 until local buckling couples with the global mode (first bifurcation point S_0). Branching at S_0 enters the post-interactive buckling stage (Stage 2), where member capacity increases slightly to the ultimate load P_u before dropping rapidly.

Based on this computational process and result data, the variation of member capacity with displacement can be determined for pre-interactive buckling, interactive buckling critical points, and post-interactive buckling stages. Additionally, continuation calculations can determine member capacity at any specific displacement. Sufficient computational accuracy can be achieved by reducing step size.

3. Model Examples

This study investigates: (1) the effect of nonlinear material mechanical properties on interactive buckling of perfect members; (2) the effect of global initial imperfections on interactive buckling. In all examples, the material hardening coefficient $n = 3$, corresponding to material strength on the lower bound of practical values [33].

3.1 Perfect Member Example

The perfect thin-walled I-section member is designated I-L3200, with geometric and material properties listed in . Torsional spring stiffness c is assumed infinite, and equation (8) is used to calculate compressed flange out-of-plane displacement. The member' s global buckling critical load $P_C \approx P_E$ (Euler load), where $P_E = \pi_{0I}^{2E}/L^2$. Plate local buckling critical stress is calculated by $\sigma = \pi^{2kD}/b^{2t}$, where b is plate width, t is plate thickness, D is plate flexural stiffness, and k depends on boundary conditions. For webs (four-edge supported) $k = 4$; for flanges (three-edge supported, one free) $k = 1.247$. Calculated critical stresses for global, flange local, and web local buckling are 93.24, 116.88, and 303.68 N/mm^2, respectively. Thus, global buckling occurs first, validating the assumption that the web does not buckle.

Load-displacement curves for different material nominal yield strengths (parameter K, as listed in) are shown in

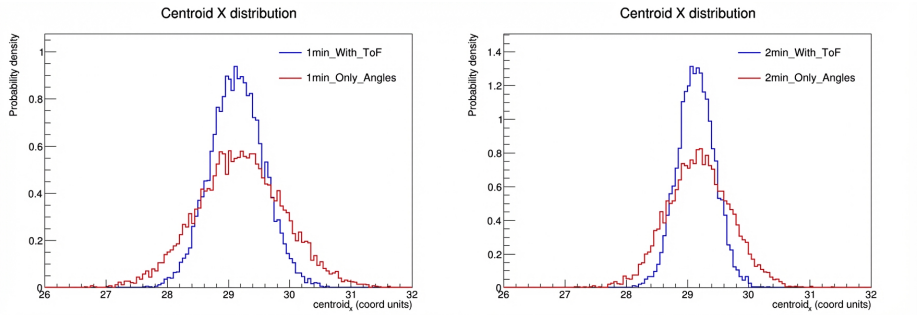

Figure 1: Figure 8

, where $p = P/P_E$ represents the dimensionless external load.

For the load-global lateral displacement curve (

(a)), members undergo global buckling at point C, reaching ultimate capacity. Between points C and S, members maintain neutral equilibrium when $K = 0$ and weak stable equilibrium when $K > 0$. Point S is the critical point for interactive buckling, after which members enter the post-interactive buckling stage with rapidly decreasing capacity. When $0.8 < p < 1.0$, the nonlinear

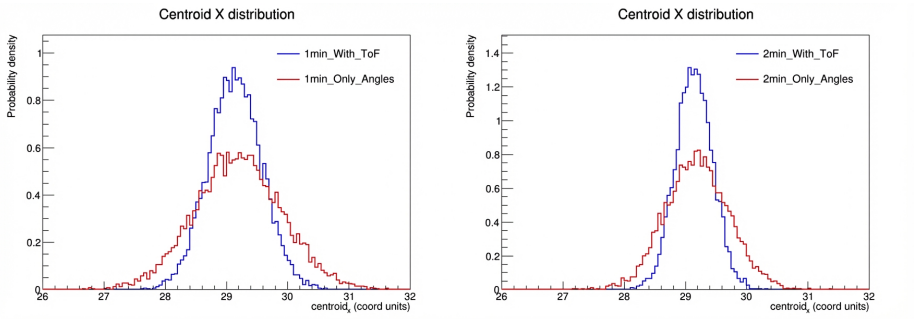

Figure 2: Figure 8

higher-order term $K(\varepsilon_L)^n$ constitutes a low proportion of strain ε, making lateral displacement W and its linear component W_L curves nearly coincident. As displacement increases, the influence of the nonlinear term becomes significant, causing divergence between W and W_L curves for the same K. Member capacity and post-interactive buckling performance decrease as material nominal yield strength decreases (parameter K increases) at the same displacement level.

Post-interactive buckling performance also correlates positively with material nominal yield strength for load-local out-of-plane displacement and load-axial displacement curves (

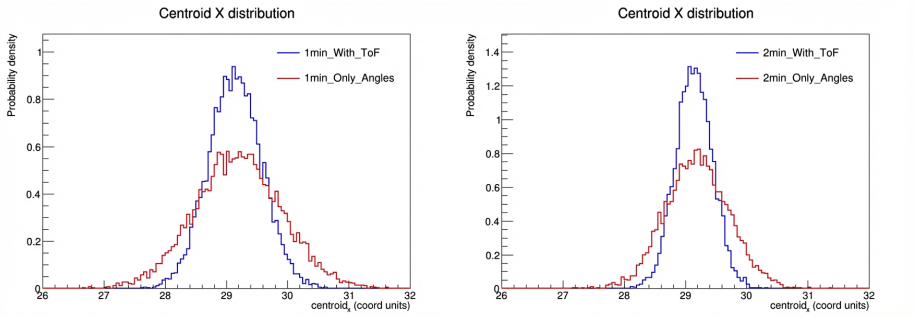

Figure 3: Figure 8

(b) and (c)). Material nonlinearity causes actual displacement to exceed its linear component at the same load level (

(a)-(c)). Additionally, the relationship between global displacement W and local displacement w is minimally affected by material nominal yield strength (

(d)).

Flange local buckling mode development under different parameters K and capacity levels is shown in [FIGURE:9]. Results indicate that in the post-

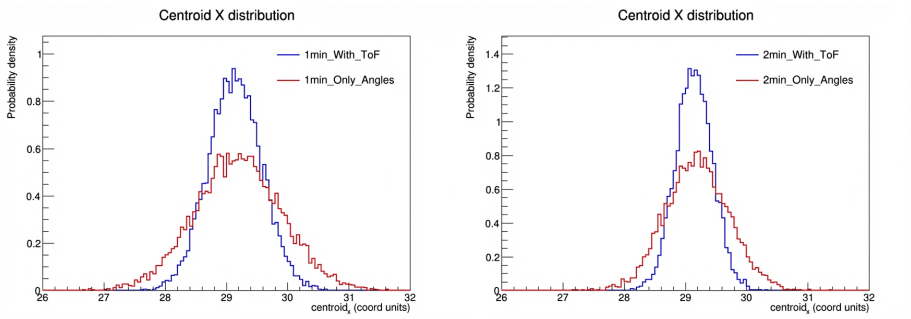

Figure 4: Figure 8

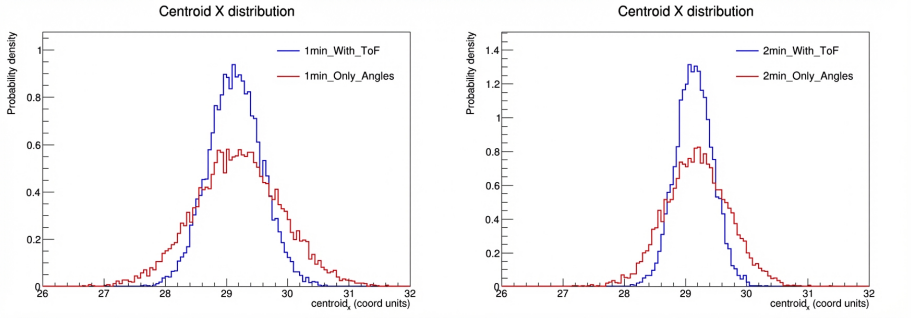

Figure 5: Figure 8

interactive buckling stage, out-of-plane displacement w amplitude increases while local buckling wavelength decreases as member capacity drops, with buckling waveforms spreading from mid-span toward ends. At the same capacity level, out-of-plane displacement w amplitude decreases as material nominal yield strength decreases.

Maximum normal strain-stress in the member at $p = 0.65$ is marked in [FIGURE:10], with nominal yield strength $\sigma_{0.2}$ and strain $\varepsilon_{0.2}$ shown as dashed lines. Even after significant post-buckling deformation development with a 35% capacity drop from the critical load, maximum normal stress remains far below nominal yield strength, indicating minimal plastic strain. Therefore, within the interactive buckling range discussed, using the original R-O model rather than the commonly used two-stage R-O model in practical engineering produces negligible error for slender members.

3.2 Member with Global Initial Imperfections Example

The member with global initial imperfections is designated I-L4000, with parameters listed in . Dimensionless ultimate capacity is defined as $p_u = P_u/P_E$. When $K = 1 \times 10^4$ and $c = 100$ Nm/m, ultimate capacities and load-displacement curves under different global initial imperfection amplitudes Q_0 are shown in and [FIGURE:11].

For members with global initial imperfections, the global bending mode occurs first under external load. As load increases, stresses in flanges increase while deformations develop until local buckling occurs and couples with the global mode. The member then reaches ultimate capacity and becomes unstable, with capacity continuously decreasing. Divergence among load-displacement curves increases with load before reaching ultimate capacity; during capacity drop stage, the distance between curves decreases with increasing displacement, and the capacity drop relative to ultimate capacity decreases with increasing global initial imperfection amplitude (FIGURE:11-(c)).

and FIGURE:11 show that member ultimate capacity is inversely proportional to global initial imperfection amplitude, with the latter significantly affecting the former. Therefore, global initial imperfections cannot be neglected in engineering practice.

4. Model Validation

This study simulates Becque' s interactive stability tests on thin-walled I-section compression members [30] using the variational model, comparing results with both Becque' s experimental and finite element simulation results [30]. Test members were formed by fastening two cold-formed 404 stainless steel C-section components. Member designations and parameters are listed in . Model parameters including material properties, flange-web connection stiffness, and global initial imperfections are first determined to match test conditions, then member model load-displacement curves are calculated.

4.1 Model Parameter Determination

Material mechanical properties for the variational model are determined by fitting the R-O formula to compressive stress-strain curves from material tests on flat regions of test members. Since maximum normal strain in slender members during post-interactive buckling is far below the total strain corresponding to $\sigma_{0.2}$, this study employs the R-O formula with the best fit to test data in the range $0 < \varepsilon < 0.2\%$, where $K = 1.5 \times 10^5$, as shown in [FIGURE:12]. Flange-web connection stiffness is determined from as $c = 500$ Nm/m. Global initial imperfections for test members I404-L3000 and I404-L2500 are obtained from measured test data. Considering transverse offset at mid-span measurement points, the average initial eccentricity e_0 of external load P relative to mid-span and end sections are $L_e/1912$ and $L_e/1645$, respectively. Therefore, dimensionless initial imperfection amplitudes Q_0 in the variational model should be 5.2×10^{-4} and 6.1×10^{-4}.

4.2 Comparison of Model Results with Experiments

For both member lengths, the variational model shows excellent agreement with test members in load-displacement curves for transverse and axial displacements throughout the interactive buckling process ([FIGURE:13]). Compared with finite element simulation, the variational model correlates better with experimental results, providing more complete analysis of post-interactive buckling displacement and capacity development. Particularly in the post-buckling capacity drop stage where large deformations occur simultaneously, material nonlinearity significantly affects instability curves. The present model accurately simulates this factor through the nonlinear term $K(\varepsilon_L)^n$, resulting in high consistency with experimental curves.

For member I404-L3000, the experimental ultimate load is approximately 24.71 kN, while the variational model predicts 25.36 kN (2.6% error). At a global lateral displacement of 40 mm, both test and model members have undergone global-local interactive buckling and are in the rapid capacity drop stage; the model capacity differs from the test by only 2.7%, significantly less than the 16.1% error from finite element simulation. At an axial displacement of approximately 2 mm, the finite element load error reaches 18.7%, while the variational model matches test data closely.

For member I404-L2500, the experimental ultimate load is approximately 30.63 kN, while the model predicts 32.46 kN (6.0% error). At a global lateral displacement of 10 mm, the model capacity differs from the test by 3.5%, compared to 13.0% finite element error. The model and experimental cross-section rotation-load post-buckling equilibrium paths remain parallel, though with larger relative error than transverse and axial displacement paths. Overall, the variational model' s validity is fully verified.

Error sources between the model and test values are discussed as follows: during loading, the tangent modulus of corner region material changes, causing actual

torsional spring stiffness to deviate from values calculated based on initial elastic modulus; test members exhibit plate local initial imperfections not considered in this study; and the variational model neglects shear strain under global buckling, increasing cross-section rotation error.

Notably, the large error between finite element and test curves in [FIGURE:13] primarily results from the finite element model considering only load initial eccentricity without accounting for member initial geometric imperfections [30].

Conclusions

1) Based on the Rayleigh-Ritz method, a variational model for interactive buckling in thin-walled I-section slender members is established, considering global initial imperfections, nonlinear material R-O model, von Kármán large deflection theory, and using torsional springs to simulate flange-web connection stiffness. Results show that for perfect members, post-interactive buckling capacity at the same displacement level correlates positively with material nominal yield strength. Plate local buckling wavelength decreases as post-buckling capacity drops. Member ultimate capacity is sensitive to global initial imperfections; when imperfection amplitude reaches $L/1000$, ultimate capacity decreases by approximately 30%.

2) This variational model fills the gap in analytical research on interactive buckling of thin-walled I-section members considering both geometric and material nonlinearities. The method is also applicable to interactive stability problems in thin-walled slender members with other flat-plate cross-sections, such as T-section, C-section, and H-section, though total potential energy functionals must be derived according to specific cross-sectional forms. Compared with finite element methods, the variational model facilitates parametric analysis requiring only parameter value modifications in program scripts. The limitation is that establishing concise and accurate theoretical variational models becomes difficult for complex cross-sections with many component plates, where finite element methods are more appropriate.

3) Variational model simulations show excellent agreement with existing experimental results. Differences between model and experimental ultimate capacities are within 6%. In the post-interactive buckling stage, percentage differences in capacity between model and experiments are even lower at the same transverse or axial displacement level.

4) After significant post-buckling capacity drop, maximum normal stress and strain remain far below $\sigma_{0.2}$ and $\varepsilon_{0.2}$, validating the effectiveness of using the original R-O model rather than a two-stage model for analyzing interactive buckling in slender members. The present model applies to interactive stability problems in slender members where design loads are controlled by global buckling critical loads, but not to short columns. For

short columns where global buckling critical stress approaches nominal yield strength, a two-stage R-O model is required.

References

[1] HANCOCK G J. Local, distortional, and lateral buckling of I-beams [J]. Journal of the structural division, 1978, 104(11): 1787-1798.
[2] SCHAFER B W. Local, distortional, and Euler buckling of thin-walled columns[J]. Journal of structural engineering, 2002, 128(3): 289-299.
[3] HANCOCK G J. Cold-formed steel structures: research review 2013–2014 [J]. Advances in structural engineering, 2016, 19(3): 393-408.
[4] CAMOTIM D, MARTINS A D, DINIS P B, et al. Mode interaction in cold-formed steel members: state-of-art report [J]. Steel construction, 2020, 13(3): 186-207.
[5] BAI L, WANG F, WADEE M A, et al. Nonlinear mode interaction in equal-leg angle struts susceptible to cellular buckling[J]. Proceedings of the Royal Society a: mathematical, physical and engineering sciences, 2017, 473(2207): 20170583.
[6] CHEN Shaobo. Recent progress in structural steel stability design [J]. Progress in steel building structures, 2004, 6(2): 1-13 (in Chinese).
[7] HU Zhizhong. Study on local-distortional interactive buckling mechanical properties of perforated high-strength cold-formed thin-walled steel columns[D]. Huainan: Anhui University of Science and Technology, 2021.
[8] LI Chenxu. Research on local and distortional interactive buckling of stainless steel lipped C-section columns[D]. Nanjing: Southeast University, 2021.
[9] REN Chong, LIU Qiuting, WANG Binhua, et al. Numerical analysis and design method of cold-formed thin-walled C-section steel perforated member[J]. Journal of Shanghai Jiao Tong University, 2020, 54(10): 1084-1093 (in Chinese).
[10] SHEN J J, WADEE M A. Length effects on interactive buckling in thin-walled rectangular hollow section struts[J]. Thin-walled structures, 2018, 128: 152-170.
[11] SHEN Hongxia. The stability of high-strength steel welded thin-walled box beam-columns under biaxial bending[J]. Progress in steel building structures, 2020, 22(4): 57-67 (in Chinese).
[12] ZHANG L L, LIANG Y T, ZHAO O. Flexural-torsional buckling behaviour and resistances of fixed-ended press-braked S690 high strength steel angle section columns[J]. Engineering structures, 2020, 223: 111180.
[13] BAI L, YANG J, WADEE M A. Cellular buckling from nonlinear mode interaction in unequal-leg angle struts[J]. Thin-walled structures, 2018, 132: 316-331.
[14] YAO Xingyou, LI Xiao. Tests and direct strength method on the distortional buckling and interactive buckling of cold-formed thin-walled steel built-up I-section columns under axial compression[J]. Progress in steel building structures, 2021, 23(12): 33-46 (in Chinese).

[15] BAI L, WADEE M A. Slenderness effects in thin-walled I-section struts susceptible to local-global mode interaction[J]. Engineering structures, 2016, 124: 128-141.
[16] TETER A, KOLAKOWSKI Z. Interactive buckling of wide plates made of functionally graded materials with rectangular stiffeners[J]. Thin-walled structures, 2022, 171: 108750.
[17] WADEE M A, FARSI M. Cellular buckling in stiffened plates[J]. Proceedings of the Royal Society a: mathematical, physical and engineering sciences, 2014, 470(2168): 20140094.
[18] GARDNER L, NETHERCOT D A. Experiments on stainless steel hollow sections—part 1: material and cross-sectional behaviour[J]. Journal of constructional steel research, 2004, 60(9): 1291-1308.
[19] GEORGANTZIA E, GKANTOU M, KAMARIS G S. Aluminium alloys as structural material: a review of research[J]. Engineering structures, 2021, 227: 111372.
[20] WANG Yuanqing, YUAN Huanxin, SHI Yongjiu, et al. A review of current applications and research of stainless steel structure[J]. Steel construction, 2010, 25(2): 1-12 (in Chinese).
[21] ZHAO J H, FAN S G, LI C X, et al. Research on the local-distortional interaction buckling capacity of stainless steel lipped C-section columns[J]. Structures, 2023, 48: 2003-2023.
[22] ROY K, HO LAU H, AHMED A M M, et al. Nonlinear behavior of cold-formed stainless steel built-up box sections under axial compression[J]. Structures, 2021, 30: 390-408.
[23] KOUNADIS A N, MALLIS J G. Elastica type buckling analysis of bars from non-linearly elastic material[J]. International journal of non-linear mechanics, 1987, 22(2): 99-107.
[24] SAETIEW W, CHUCHEEPSAKUL S. Post-buckling of linearly tapered column made of nonlinear elastic materials obeying the generalized Ludwick constitutive law[J]. International journal of mechanical sciences, 2012, 65(1): 83-96.
[25] RAMBERG W, OSGOOD W R. Description of stress-strain curves by three parameters[EB/OL]. (1943-07-01)[2022-09-12]. https://ntrs.nasa.gov/citations/19930081614.
[26] BAI L, WADEE M A, KÖLLNER A, et al. Variational modelling of local-global mode interaction in long rectangular hollow section struts with ramberg-osgood type material nonlinearity[J]. International journal of mechanical sciences, 2021, 209: 106691.
[27] WADEE M A, BAI L. Cellular buckling in I-section struts[J]. Thin-walled structures, 2014, 81: 89-100.
[28] BAI L, WADEE M A. Imperfection sensitivity of thin-walled I-section struts susceptible to cellular buckling[J]. International journal of mechanical sciences, 2015, 104: 162-173.
[29] BAI L, WADEE M A. Mode interaction in thin-walled I-section struts with semi-rigid flange-web joints[J]. International journal of non-linear mechanics, 2015, 69: 71-83.
[30] BECQUE J. The interaction of local and overall buckling of cold-formed

stainless steel columns[D]. Sydney: University of Sydney, 2009.
[31] HILL H N. Determination of stress-strain relations from "offset" yield strength values[EB/OL]. (1944-02-01)[2022-09-14]. https://ntrs.nasa.gov/citations/19930081673.
[32] DOEDEL E, CHAMPNEYS A, DERCOLE F, et al. Auto: software for continuation and bifurcation problems in ordinary differential equations[EB/OL]. (2019-11-30)[2022-11-24]. http://indy.cs.concordia.ca/auto/.
[33] KAMAYA M. Ramberg-Osgood type stress-strain curve estimation using yield and ultimate strengths for failure assessments[J]. International journal of pressure vessels and piping, 2016, 137: 1-12.